MATERIALS SCIENCE

# Subnanosecond phase transition dynamics in laser-shocked iron



H. Hwang[1], E. Galtier[2], H. Cynn[3], I. Eom[4], S. H. Chun[4], Y. Bang[1], G. C. Hwang[1], J. Choi[1], T. Kim[1], M. Kong[1], S. Kwon[1], K. Kang[1], H. J. Lee[2], C. Park[5], J. I. Lee[5], Yongmoon Lee[6], W. Yang[6], S.-H. Shim[7], T. Vogt[8], Sangsoo Kim[4], J. Park[4], Sunam Kim[4], D. Nam[4], J. H. Lee[4], H. Hyun[4], M. Kim[4], T.-Y. Koo[4], C.-C. Kao[2], T. Sekine[6,9], Yongjae Lee[1,6]*



**Iron is one of the most studied chemical elements due to its sociotechnological and planetary importance; hence, understanding its structural transition dynamics is of vital interest. By combining a short pulse optical laser and an ultrashort free electron laser pulse, we have observed the subnanosecond structural dynamics of iron from high-quality x-ray diffraction data measured at 50-ps intervals up to 2500 ps. We unequivocally identify a three-wave structure during the initial compression and a two-wave structure during the decaying shock, involving all of the known structural types of iron (α-, γ-, and ε-phase). In the final stage, negative lattice pressures are generated by the propagation of rarefaction waves, leading to the formation of expanded phases and the recovery of γ-phase. Our observations demonstrate the unique capability of measuring the atomistic evolution during the entire lattice compression and release processes at unprecedented time and strain rate.**

## INTRODUCTION

Iron is the most stable and heaviest chemical element produced by nucleosynthesis in stars, making it the most abundant heavy element in the universe and, hence, in the interiors of Earth and other rocky planets (*1*–*3*). The high-pressure behavior of iron is therefore of enormous importance to better understand the physics and chemistry and the magnetic properties of Earth and other planets (*4*). Because of the accessible pressure range of its phase transitions, iron has also been an archetypical material for high-pressure studies in early static diamond anvil cell (*1*) and dynamic compression experiments (*2*). This triggered the pressure-dependent investigations of many important physical and chemical properties such as magnetic-to-nonmagnetic phase transition with large hysteresis (*5*, *6*), kinetics (*7*), volume collapse (*8*), and characterization of the triple point (*9*, *10*), as well as the sensitivity of mechanical properties to microstructures and strain rate (*11*). At ambient conditions, metallic iron is stable as a body-centered cubic (bcc) form (α-phase) with ferromagnetic ordering. At pressures above ca. 13 GPa, about 130,000 times the atmospheric pressure, iron transforms to a nonmagnetic hexagonal close-packed (hcp) structure (ε-phase) (*12*–*14*). This transformation is martensitic (i.e., diffusionless), and one observes a coexistence of the α- and ε-phase. There are still debates about the locations of the phase boundaries in the phase diagram as well as the kinetics of this phase transition.

Shock compression via optical lasers or gas guns provides a unique opportunity to study the dynamics of materials and has been of particular interest to understand shock propagation, impact processes, and the presence of metastable phases associated with structural transformations. In the 1950s, a phase transition was first detected in shocked iron (*15*, *16*). To explain this phase transition, a dynamic evolution of the iron lattice from a one-dimensional (1D) elastic to a 3D plastically relaxed state within a few nanoseconds was proposed (*17*). Barker and Hollenbach (*7*) used a time-resolved velocity interferometer system for any reflector (VISAR) to study the phase transition kinetics in shocked iron and identified three distinct shock waves: an elastic (E), a plastic (P1), and a phase transforming wave (P2) (*7*, *15*, *16*). In contrast to the proposed three deformation waves, split two shock waves inducing a direct α-phase–to–ε-phase transition of iron has been suggested by Kadau *et al.* (*18*), who simulated a perfect single crystal without defects and found no evidence of a P2 wave in a million-atom molecular dynamic simulation. Kadau *et al.* (*17*) also claimed that the α-phase–to–ε-phase transformation threshold time can be shorter than 60 ps for iron with defects and heterogeneous nucleation. Jensen *et al.* (*19*) claimed remarkably similar wave profiles as Barker and Hollenbach (*7*), showing the typical three shock waves and similar peak particle velocity at arrival times for the P2 wave. These suggest that a pump-probe experiment at every 50-ps delay time or less would be adequate to observe these transformations.

The first direct experimental observations of crystallographic structures of shocked iron were made only recently in 2005 by Kalantar *et al.* (*20*). Until then, it was assumed that the transition inferred from the wave profiles of shocked iron would be the same as the one measured in static experiments (*12*). Using several tens-of-nanosecond-long x-ray pulses, Johnson *et al.* (*21*–*23*) experimentally measured Bragg diffraction from a shocked iron crystal. With high-intensity lasers to create a subnanosecond x-ray source, x-ray diffraction (XRD) from laser-shocked crystals became available, and the dynamic response during shock compression could be investigated (*24*). The high-intensity laser could generate enough x-ray photons in a short burst to act as an x-ray source (a so-called backlighter) for XRD with a brightness greater than those of the third-generation synchrotron sources. Hawreliak *et al.* (*25*) used the OMEGA, Janus, and Vulcan laser facilities to study the phase transition mechanism from α to ε iron (*25*–*27*). Bastea *et al.* (*28*) used the Sandia Z accelerator to study kinetic features of ramp compressed iron and conjectured

[1]Department of Earth System Sciences, Yonsei University, Seoul 03722, Republic of Korea. [2]Linac Coherent Light Source, SLAC National Accelerator Laboratory, Menlo Park, CA 94025, USA. [3]High Pressure Physics Group, Lawrence Livermore National Laboratory, Livermore, CA 94550, USA. [4]Pohang Accelerator Laboratory, Pohang, Gyeongbuk 37673, Republic of Korea. [5]Korea Polar Research Institute, Incheon 21990, Republic of Korea. [6]Center for High Pressure Science and Technology Advanced Research, Shanghai 201203, China. [7]School of Earth and Space Exploration, Arizona State University, Tempe, AZ 85287, USA. [8]NanoCenter and Department of Chemistry and Biochemistry, University of South Carolina, Columbia, SC 29208, USA. [9]Graduate School of Engineering, Osaka University, Suita, Osaka 565-0871, Japan.
*Corresponding author. Email: yongjaelee@yonsei.ac.kr

that overshoot (velocity loop) of the P1 wave may occur at a faster compression rate. Jensen *et al.* (*19*) also addressed kinetics of shocked iron using plate impact and determined that the phase transition stress from α to ε iron for a single crystal and powder was different, i.e., 14.26 and 12.89 GPa, respectively. Crowhurst *et al.* (*29*) used a laser pulse drive to compress iron foil and measured free surface velocities. They reported that the phase transition from α to ε iron begins within 100 ps right after elastic compression. In addition, recent molecular dynamic simulations of iron suggest the formation of a face-centered cubic (fcc) form (γ-phase) by shock compression at ~40 GPa (*30*). Over the past decades, advances in extremely bright x-ray sources, like the x-ray free electron lasers (XFEL) provided previously unknown capabilities to explore not only the structural changes of compressed material but also the dynamics of these phase transitions with high temporal resolution (*31*, *32*). It is unexpected that iron has not been studied yet using any XFEL sources despite its paradigmatic importance and discrepancies in understanding its phase transition dynamics.

Here, we report the unique combination of an optical laser pump and XFEL probe to observe the atomic structural evolution of shock-compressed iron at an unprecedented time resolution, ~ 50 ps under high strain rate. We observed the three-wave temporal evolution by the elastic (E), plastic (P1), and the deformational phase transition to ε-phase (P2), followed by postcompression phases due to rarefaction waves in 50-ps intervals between 0 and 2.5 ns after irradiation with the optical laser. This is the first direct and complete observation of shock wave propagation associated with the crystal structural changes recorded by high-quality time series XRD data.

## RESULTS

The experiment was performed at the hard x-ray beamline XSS (x-ray scattering and spectroscopy) at Pohang Accelerator Laboratory X-ray Free Electron Laser (PAL-XFEL) in Pohang, Korea. As shown in Fig. 1, 4-μm-thick polycrystalline Fe foils (99.9% pure synthetic iron) were illuminated at ~5° to the surface normal by an 800-nm wavelength Ti:sapphire laser chirped to 140 ps with an energy of 6.1 mJ, focused down to a 40-μm-diameter spot on the sample surface (see Materials and Methods). The iron sample was probed by a 25-fs quasi-monochromatic (bandwidth 0.4%) x-ray pulse at a photon energy of 12 keV with $10^{11}$ photons per pulse. The femtosecond x-ray pulse allows us to take instantaneous snapshots of the atomic structure of the sample with dynamics faster than picoseconds, which is already too fast to see any thermodynamic processes. The x-ray beam was focused down to a 20-μm-diameter spot on the sample using Be compound refractive lenses (CRL) available at the beamline. A cartridge that could contain up to 4 × 4 thin Fe foils (disks of 5-mm diameters) was translated for single-shot measurements by a linear stage mounted on a hexapod. The iron target was normal to the x-ray pulse, with the diffraction detector in transmission geometry (Fig. 1). Since the attenuation length of Fe at 12 keV is ca. 6.85 μm, x-ray photons are diffracted along the full depth of the 4-μm-thick Fe foil, allowing the observation of all the atomic structures of the entire sample with expected diffraction intensity and its possible mixed phases due to the martensic nature of some of the iron phase transitions. Arcs of the α-phase (110), (200), (211), (220), (310), and (222) Debye-Scherrer rings were observed in a single shot using a Rayonix MX225-HS detector placed at a distance of about 22 cm from the sample covering 2θ angles up to 72° (more details in Materials and Methods).

The optical laser and the x-ray laser were synchronized to allow XRD patterns to be recorded in 50-ps (or 100) intervals up to a 2.5-ns delay time after the onset of irradiation by the optical laser. Figure 2 shows single-shot diffraction images at selected delay times of 0, 250, 500, 700, and 1200 ps, where one can identify α-phase at ambient conditions, at the Hugoniot elastic limit (HEL) (E), when the plastic compression (P1) occurs, and ε-phase of iron when the high-pressure phase (P2) forms. Rarefaction waves are present at later stages, as evidenced by the released α-phase and newly formed γ-phases as well as their expanded states (Fig. 2 and fig. S1). The high-quality diffraction data enable us to investigate the full structural and temporal evolution of shock-compressed iron.

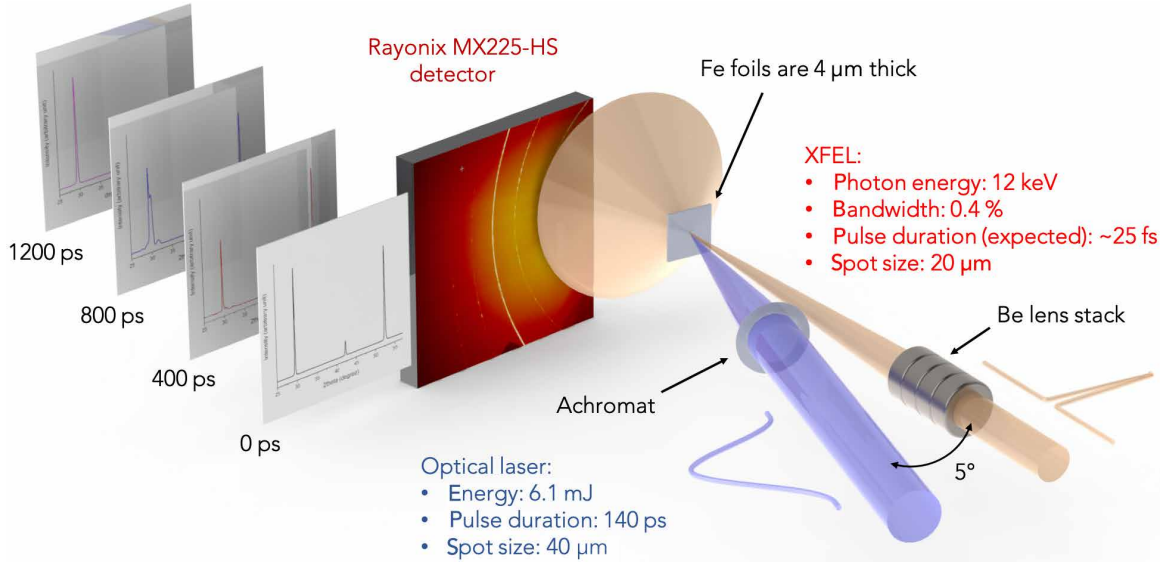


**Fig. 1. Experimental configuration of the laser pump and XFEL probe setup.** The polycrystalline iron target is illuminated by an optical pump laser. Lattice spacings of the target are probed by the XFEL beam in transmission geometry.

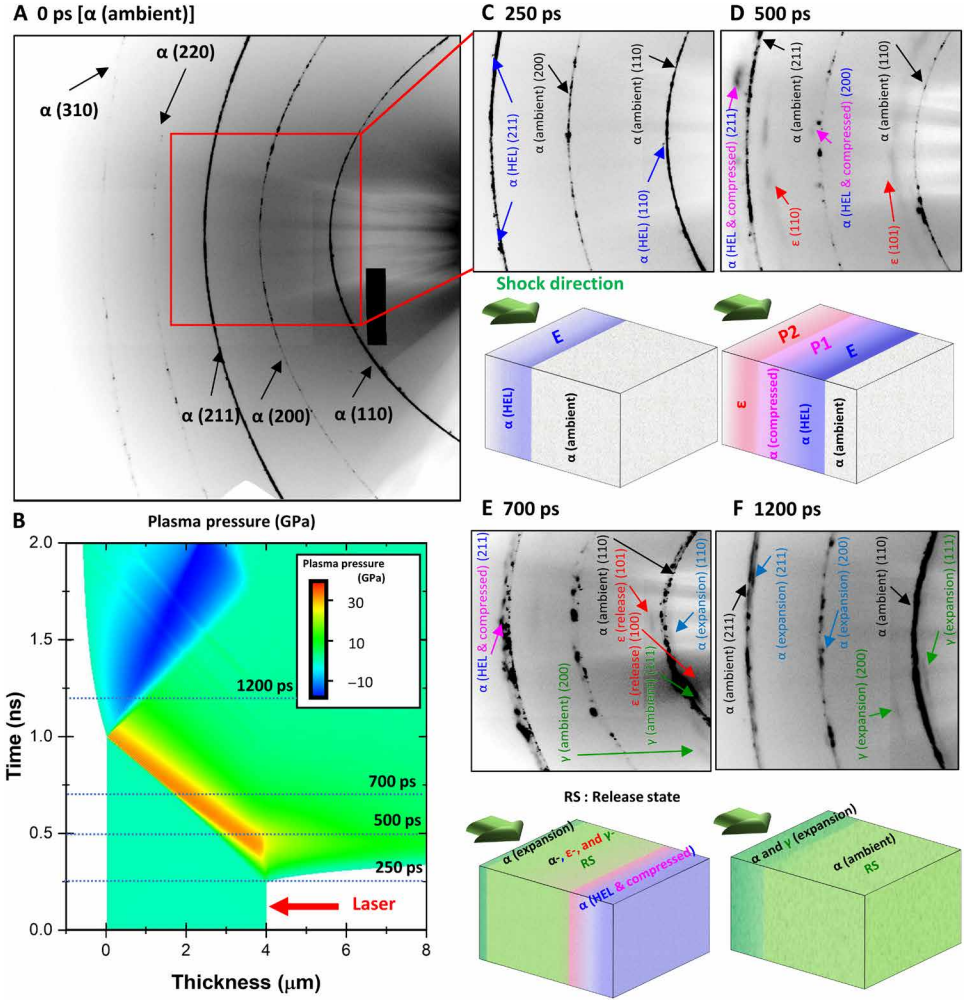


**Fig. 2. Diffraction images of laser-shocked 4-μm-thick iron at selected delay times with schematic illustrations of corresponding shock propagation.** (**A**) Debye-Scherrer rings of α-phase (110), (200), (211), (220), and (310) reflections with a marginal trace from (222) peak at ambient conditions (0 ps). (**B**) 1D hydrodynamic HELIOS-CR simulation showing the expected breakout time at the rear surface of the sample. Diffraction images and corresponding shock propagation stages at delay times of (**C**) 250, (**D**) 500, (**E**) 700, and (**F**) 1200 ps.

Time series diffraction data were processed using the Dioptas software (*33*). The indexing of the peaks at selected delay times and the calculated densities as a function of delay time are shown in Figs. 3 and 4, respectively. In all the measured diffraction data, we observe sharp α-phase peaks with the strongest (110) diffraction near 29.6° (ambient iron with an average density of 7.89 g/cm$^3$). Initially, α-phase in the HEL occurs at times between 250 and 600 ps with an average density of 8.10 g/cm$^3$, which is followed by compressed α-phase (P1; 8.47 g/cm$^3$) and high-pressure ε-phase (P2; 9.18 g/cm$^3$) peaks at times between 300 and 600 ps. During this time, peak stress is observed near 450 ps to be ~34 GPa with a corresponding strain rate of ~$3.0 \times 10^9$ s$^{-1}$ (*34*, *35*). The strain rate was calculated using the equation defining the strain rate presented in Smith *et al*. (*8*). The compressive strain rate associated with the phase transformation was described as

$$\dot{\mu} = \frac{1}{\rho_0}\frac{\Delta\rho}{\Delta t}$$

where $\dot{\mu}$ is the compressive strain rate on phase transition, $\rho_0$ is the density of ambient α-phase taken at 0 ps, $\Delta\rho$ is the difference of density between α- and ε-phase, and $\Delta t$ is the time gap on phase transition from α-phase to ε-phase. After this stage, ε-phase with a lower density (8.68 g/cm$^3$) is observed between 650 and 850 ps, which partially overlaps with α-phase (8.25 g/cm$^3$) and HEL (8.04 g/cm$^3$) during decaying shock compressions that occur at times between 650 and 1100 ps (Fig. 4). This corresponds to the hysteresis of the back transformation of the ε-phase. All the compressed ε- and α-phase of iron disappear after 850 and 1100 ps, respectively.

Close examination of the peaks reveals the appearance of new phases after 650 ps with densities similar or even lower than that of ambient α-phase. Figure 3B shows the detailed analysis of the shoulder peaks as well as weak ones above the background level, assigned collectively to the γ-phase and the expanded α-phase at a delay time of 700 ps. The newly formed γ-phase exhibits an average density of 7.93 g/cm$^3$ between 650 and 900 ps, similar to that of the α-phase at ambient pressure. After 900 ps, the unit cell volume of the γ-phase expands by ca. 3.9%, corresponding to a decrease in density to

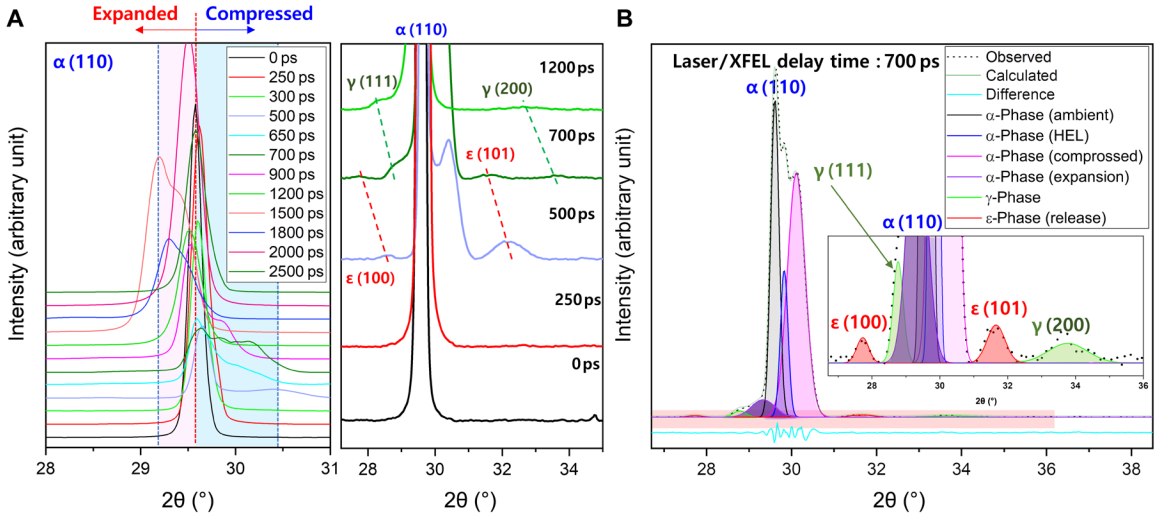


**Fig. 3. Changes in the diffraction patterns of 4-μm-thick iron as a function of delay time from laser shock.** (**A**) The (110) reflection intensity of α-phase at ambient conditions (0 ps) starts to decrease at 250 ps with the emergence of additional reflection features dominating at the high 2θ angle side up to 700 ps, after which new diffraction peaks evolve as shoulders of the α (110) at the low 2θ angle side up to 2000 ps. Assignments of ε- and γ-phase peaks are shown in the middle in the enlarged view. (**B**) Pseudo-Voigt profile fitting of the diffraction pattern measured at 700-ps delay time. The major (110) reflection of α-phase is composed of ambient, compressed (HEL and released P1), and an expanded quadruplet. Inset shows the existence of ε-phase (released P2) and γ-phase (ambient) above the background level. Profile fittings at different delay times are shown in fig. S1.

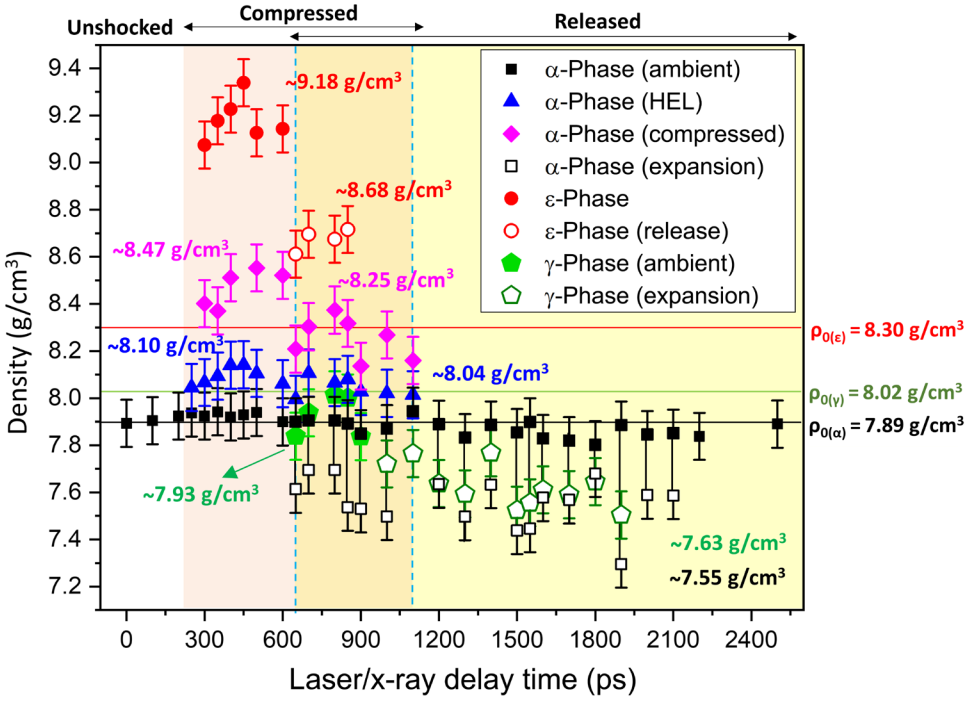


**Fig. 4. Time series lattice response of 4-μm-thick shocked iron at delay times between 0 and 2.5 ns.** Density was calculated based on the refined positions of diffraction peaks over 24 and 58 in 2θ. There are three different structural types of iron phases (α-, ε-, and γ-phase). The compressed states consist of α- and ε-phase. Only the elastic compression state is observed at 250 ps, after which three-wave structures coexist between 300 and 600 ps. A compressed α-phase with partially released states of ε- and γ-phase then evolve from 650 to 1100 ps. After 1100 ps, no compressed states are seen, but expanded α- and γ-phase are observed up to 2100 ps. At the final delay times of 2200 and 2500 ps, only the ambient α-phase is observed.

7.63 g/cm$^3$. This expanded γ-phase then persists up to 1900 ps. On the other hand, the expanded α-phase formed at 650 ps exhibits an average density of 7.55 g/cm$^3$, which is ca. 4.5% lower than that of α-phase at ambient conditions and persists up to 2100 ps. After 2100 ps, only the ambient α-phase remains up to the final delay time of 2500 ps.

According to our 1D hydrocode simulations (Fig. 2B and fig. S2), the high-pressure compression stage ends about 600 ps, after which the release process follows (see Materials and Methods for more details on the hydrodynamic simulations). Taking into account the 3D effects due to the relative size of our optical laser beam (~40 μm)

compared with the XFEL beam (~20 μm), the radial rarefaction will reach the edge of the XFEL beam earlier than from the optical laser side. These effects will give us a chance to look at the release processes as well as compression. The less dense α-phase indicates negative stresses of ~8(2) GPa, when calculated based on the shock Hugoniot and isentropic release (*34*, *35*). Although there are no direct temperature diagnostics, we suspect that there is no significant sample preheating in our experiments due to the relatively low laser pump intensity (~6.1 mJ). We did not detect any expansion of α-phase before compression (Fig. 4), although preheating and initial expansion have been reported in Au foil using a pump laser with a pulse energy of 1 J (*36*).

On the basis of our diffraction results, the laser shock stress decays significantly during their propagation, as seen in fig. S3 and table S1 (*34*, *35*). When the high-pressure ε-phase (P2) is present between 300 and 600 ps with an average density of 9.18 g/cm$^3$ and a peak stress of ca. 34 GPa, the second phase of compressed α-phase (P1) maintains a constant density of 8.47 g/cm$^3$ at an average stress of ca. 13.6 GPa that supports the phase transition, while the initial elastic phase (E) shows an average density of 8.10 g/cm$^3$ at an average stress of ca. 7.6 GPa. The partially released states of the ε- and γ-phase at times between 650 and 850 ps and 650 and 900 ps, respectively, are coexisting with lower-density α-phase than that found at ambient conditions. The peak stress decays rapidly, and no compressed phases are present after 1100 ps. During this release process, the stress level observed by the XFEL would consist of two states, i.e., the central part, which relaxes toward ambient conditions, and the edge part subjected to further radial rarefaction.

The crystallite sizes estimated from the measured diffraction peak widths are plotted in fig. S4 to reveal the comminution effect associated with the propagation of shock and rarefaction waves. In the initial compression stage, all of the three waves exhibit increases in their diffraction peak widths and, hence, a decrease in crystallite sizes in the order of the HEL (E), the compressed α-phase (P1), and the high-pressure ε-phase (P2), which consists of the tiniest grains of ca. 0.04 μm (table S1). During the release processes, the expanded α- and γ-phases maintain smaller grain sizes, indicating a rapid recrystallization, while the recovered α-phase appears to revert closely to the original grain sizes of ca. 0.34 μm.

Previous studies have probed the wave profiles for shocked iron at pressures above the phase transition (~13 GPa), where the HEL stress was not very high (below ~1 GPa) (*7*, *18*). However, recent laser shock experiments showed much higher HEL stress (~10 GPa) for thinner iron samples, where the second plastic wave merged with the wave profile of the free surface (*37*). In our data, at an early delay time of 250 ps, only the HEL (~7.2 GPa) is present without the plastically compressed α-phase state. A three-wave sequence is then observed in the diffraction pattern starting at 300 ps. These results reveal that in the shock dynamics of iron, the wave sequence depends on the HEL level and peak stress.

## DISCUSSION

In this study, we have successfully observed distinct compression states associated with a three-wave structure in polycrystalline iron and detected materials in tensile strain as a dynamical and intermediate state during the release process. The phase transition pressure between the α- and ε-phase is estimated to be 13.6 GPa and agrees with the one established from static compression experiments, although it may increase with increasing strain rate or decrease with increasing shear present. Our estimated HEL stress reaches up to ~9 GPa, which is among the highest thus far reported for shock Hugoniot of iron (fig. S3). After the peak pressure of ~34 GPa, the high-pressure ε-phase undergoes release processes and crosses the phase boundary toward the α-phase via successive volume increases to form the partially released ε-phase and the ambient γ-phase. This has to be accommodated without the formation of voids in the lattice (fig. S6). The structural difference between the ε-phase and the γ-phase is in

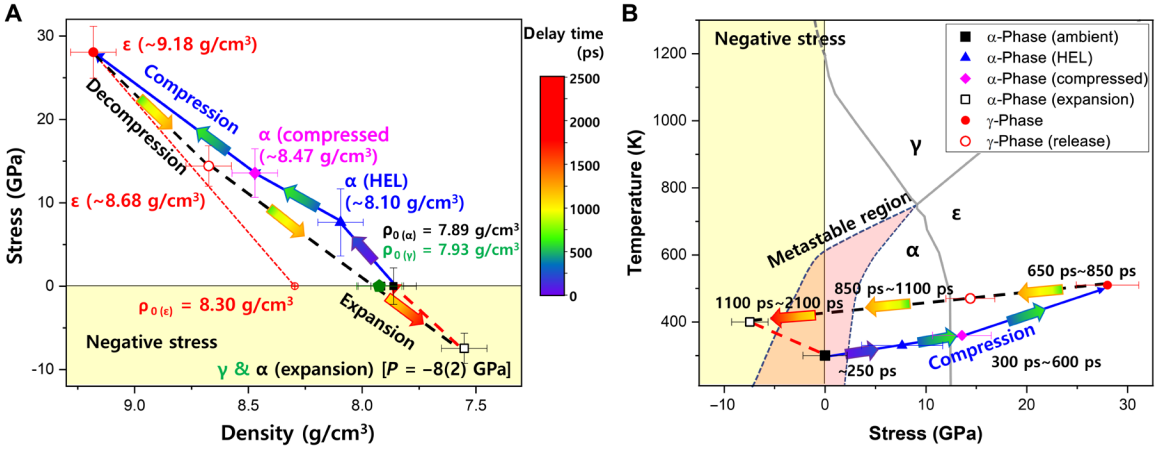


**Fig. 5. Evolution of the α- (bcc), ε- (hcp), and γ-phase (fcc) in shocked iron and the existence of a metastable γ-phase after the shock experiment.** (**A** and **B**) Schematic processes for shocked iron with experimentally determined states of the α-, ε-, and γ-phase. The arrows indicate increase in delay time. Note the boundary between α-phase and ε-phase and a possible metastable extension of the boundary between ε-phase and γ-phase from high temperatures. Solid and broken lines denote compression and decompression paths, respectively. The triple point of α-ε-γ iron is taken from the data of Dewaele *et al.* (*10*). Stress and temperature were estimated from diffraction data using the $U_s$-$U_p$ relation (see fig. S3). The calculated temperature for α-phase (HEL), α-phase, and ε-phase is taken from the theoretical Hugoniot of iron from Boettger and Wallace (*48*). The temperature at the release state ($T_R$) is on the isentrope from the Hugoniot and is given by the equation using the volume at the release state ($V$) $T_R = T_H \exp\left\{\int_V^{V_H} (\gamma/V)\,dV\right\}$ where $T_H$ and $V_H$ are temperature and volume at the Hugoniot, and γ is the Grunisen parameter. These calculated temperatures at the Hugoniot and release states are below the γ-phase stability field.

the layer sequence, ABAB… and ABCABC…, respectively. The ultrafast measurements at 50-ps intervals were sufficient to detect the temporal appearance of the ambient γ-phase (Figs. 4 and 5).

Changes in volume by rarefaction processes could be accommodated by a further expansion of the α-phase as indicated in Fig. 5. At early times, the elastic wave emerges first, and then the second plastic and phase transformation waves are seen within ~50 ps. The edge of the sample is subjected to the rarefaction wave, while the decaying shock decreases the stress rapidly. This induces partially released states by the presence of metastable ε- and α-phase, ambient γ-phase, and expanded α-phase at times between 650 and 850 ps. Between 850 and 1100 ps, only the central end is compressed, and after 1100 ps, completely released and expanded states are observed. The expanded α-phase then acts to generate negative pressure and subsequently induces the formation of the expanded γ-phase. After the delay time of 2100 ps, the ambient α-phase is the sole phase present but would be subjected to marginal thermal expansion (Figs. 4 and 5), since the transformation of the γ- to the α-phase is exothermic. Previous molecular dynamics simulations indicate that the γ-phase is formed during the compression process together with the ε-phase (*17*). Our experimental results, however, suggest that the γ-phase is metastable and can be quenched from the ε-phase. We have performed XRD grid scans around the hole made by the XFEL pulse and found the existence of a quenched γ-phase at a maximum intensity ratio of ca. 9% compared with the ambient α-phase (fig. S7). Furthermore, it has been known that shocked polycrystalline metals display dispersion in particle velocity that can cause turbulence and local temperature rise (*38*). This may occur not only during compression but also after release. Local hotspots may thus form, especially on the free surface, inducing oxidation reactions. After our maximum probing time of 2500 ps, significant local frictional heating between grains would have occurred, as was detected in the form of wüstite around the damaged hole of the recovered sample (fig. S7).

Shock-assisted and shock-induced chemical reactions are essential parts of explosive detonations (*39*) as well as promising tools in solid-state chemistry (*40*, *41*). However, the design of these ultrafast chemical reactions has been hampered by the lack of understanding of the time-dependent structural evolution. Our work on iron reveals the complex time-dependent structural changes during laser shocks thanks to the fast pump laser and ultrafast x-ray pulse from an XFEL. Triggering laser shock–induced or laser shock–assisted solid-solid or solid-gas chemical reactions after certain delay times might provide new opportunities to achieve unprecedented conversion rates and product selectivity, provided that one has characterized the structural dynamics of the reactants and the recovery of metastable phases, as demonstrated by our work.

## MATERIALS AND METHODS

### Optical laser

Uncompressed chirped pulses at 800 nm [bandwidth, 14 nm (full width at half maximum, FWHM); pulse duration, 140 ps] from Ti:sapphire amplifier (Legend Elite Duo HE+, Coherent Inc.) were used as a pump to generate the shock wave (*42*). Repetition rate of the amplifier was reduced to 10 Hz. The laser delivered 6.1 mJ on target with a shot-to-shot pulse energy stability of ~0.4% root mean square (RMS), and the intensity ratio of the prepulse to the main pulse was ~1%. The pulse duration is 140 ps measured at the FWHM of the Gaussian profile. The arrival time jitter between the optical laser and the x-ray pulses was measured to be ~25 fs (RMS) (*43*). The optical laser was synchronized with the x-ray beam by overlapping the maximum of both the beam signals of the same diode placed at the interaction point. This time overlap defined the time "zero" used in the delay between the pump and the probe beams. The 10-mm-diameter laser beam was focused on the sample with a lens of 250-mm focal length. The measured spot at the interaction point was a Gaussian profile of ~40-μm diameter (FWHM) at an incidence angle between the pump and XFEL probe set to 5° (see Fig. 1). Each diffraction data originates from a single x-ray pulse diffracting off a single optical laser shot iron sample. Fresh material was used for any new shots by translating the target.

### Wide-angle x-ray scattering experiment

The experiment was carried out in the transmission WAXS (wide-angle x-ray scattering) geometry. The x-rays were tuned to a maximum flux (about ~$2 \times 10^{11}$ photons per pulse) at 12 keV (bandwidth, FWHM 0.4%; pulse duration, ~25 fs; and repetition rate, 10 Hz), and the spot size at the sample position was ~20-μm diameter (FWHM) focused using a beryllium CRL (*44*), which gave the position stability of ~4.6 μm in horizontal and ~ 2.3 μm in vertical (*45*). This size is ca. 1/2 of the optical laser spot size, suited for observing the sample response to the laser shock. To ensure the spatial overlap of the x-ray and optical laser on the sample, a long-working distance microscope was placed near the sample and used for monitoring both beam spots. The overlap point was marked on the microscope camera and was checked periodically during the experimental campaign. The sample plane positioning was reproducible to within the depth of focus of the objective microscope, which was about 2 μm. The near colinear optical alignment to the x-ray beam geometry (5°) and the large Rayleigh length of the focused laser beam (about 3 cm) allowed us to have negligible errors in the longitudinal overlap of the beams. To check the alignment of the optical laser and XFEL positions, test shots were made on an Si wafer, which is located on the same plane as the surface of the iron sample before each shot. The lateral overlap was checked at every shot by using a microscope objective of ×20 magnification, giving a spatial resolution of less than 1 μm, which is much smaller than both laser and x-ray spot sizes.

The sample stage consists of sample holder cartridges (3-mm diameter holes in a 4 × 4 grid), linear motor stages, and a hexapod. This allows for mounting multiple samples and translating each of them to the spatial overlap point without disturbing the x-ray and laser alignments. The time delay between x-ray and optical laser pulses was set by a linear stage position that changes the path length of the laser. The single-shot x-ray image was obtained using a 2D area detector, Rayonix MX225-HS (effective area of 22.5 cm by 22.5 cm). The detector frame rate was 33 Hz, matching the repetition rates of the x-ray and optical laser pulse. A single frame with a time window of 33 ms (exposure time. 32 ms; frame transfer time, 1 ms) captures a single shot diffraction image. The detector was positioned to cover arcs of the six peaks of (110), (200), (211), (220), (310), and (222) in α-phase of iron. Debye-Scherrer rings from the sample were calibrated by fitting diffraction peaks of a $CeO_2$ (SRM 674b) standard sample using Dioptas (*33*). It was operated in the 4 × 4 binning mode (number of pixels, 1440 × 1440 effective pixel size, 156 μm× 156 μm), which provides enough momentum resolution to observe the three-wave states in shock-compressed iron. Two or three single shots at the same laser/x-ray delay time were repeatedly measured to check the reproducibility of the compression and relaxation effects.

In addition, to ensure statistically meaningful measurements, separate runs were made under slightly different sample and/or pump-probe conditions. Figure S5 demonstrates that the overall lattice dynamics of iron during shock compression and relaxation stages are consistent between different measurements, showing a similar sequence of phase evolution up to 2000-ps delay time.

### SE and BES imaging

To probe the laser-shocked regions after XFEL experiments, we measured secondary electron (SE) and backscattered electron (BSE) images using a JEOL JXA-8530F field emission electron microanalyzer at the Korea Polar Research Institute, with an accelerating voltage of 10 kV and a focused beam of 10 nA.

### Grid scanning for laser-shocked region using synchrotron XRD

Synchrotron XRD was performed on the recovered iron sample at beamline 16-IDB of the High Pressure Collaborative Access Team (HPCAT) at the Advanced Photon Source at Argonne National Laboratory. Monochromatic x-ray of 0.4066(1)Å wavelength was focused to 5 μm (horizontal) × 5 μm (vertical) in size using Kirkpatrick-Baez mirrors, and a Pilatus 1M detector was used for diffraction measurement. A sample area of 50 μm by 50 μm around the central XFEL hole was scanned in a 5-μm step using 2-s exposure time per step.

### Hydrodynamic simulations

We used a 1D hydrodynamic code, HELIOS Collisional-Radiative (*46*), to gain information on the initial shock wave propagation, decay rate, and expected pressure before release to guide the design of the experiment. In this simulation, the optical laser is a Gaussian profile of 150-ps FWHM with its maximum at 400 ps from $t = 0$ s. The numerical laser peak intensity $I_{0n}$ is derived from the measured laser peak energy $I_0$ using the laser pulse duration, laser pulse energy, and spot size on target. To take into account 3D effects due to the laser deposition geometry (essentially, a spherical blast wave), $I_{0n}$ in the code has been corrected by benchmarking the simulated pressure in the initial shock propagation phase through the uncompressed iron foil with the determined pressure using the Rankine-Hugoniot relation derived from the XRD data when the maximum pressure has been reached, for forming ε-phase at about 34 GPa and 450-ps delay. While the phase transition properties in the experiment are not being accounted for in this hydrodynamic code, the shock breakout time at the rear surface of the foil and the initial decay rate through the sample can be inferred from it. The multiplicative coefficient from the measured laser intensity $I_0$ (see "Optical laser" section) is about 1/4 such that $I_{0n} = I_0 * 1/4$. The iron foil equation of states has been calculated using the quotidian equation of state (QEOS) (*47*) model implementation in PROPACEOS (*46*) with both sides being allowed to expand. The simulation shows that the initial shock wave reaches the back of a 4-μm-thick iron foil in about 600 ps from the maximum of the laser pulse (the maximum of the laser pulse is defined as input parameter in the code, and it has been defined to be at 400 ps from $t = 0$ s in the simulation to properly take into account the rising edge of the Gaussian profile of the laser pulse shape). During the experiment, the timing of the x-rays and the optical lasers has been defined the same way, where the maximum of the temporal Gaussian profile of each pulse overlaps. It means that 0-ps delay in the experiment is when the two pulses exactly overlap at their maximum in time (which is also convolved with the response of the fast photodiode used for this measurement, of about 20 ps), and we have applied a −400-ps offset to the simulation time to compare it with the experiment. This number is independent of the experimental data and corroborates well with the observation of the rarefaction wave occurring at 600 ps in the experiment (see Fig. 4 and the earliest release time boundary). In addition, the expected maximum density at ~34 GPa extracted from the XRD is about 9.2 g/cm$^3$, which agrees well with the mass density at 450 ps in the simulation.

## SUPPLEMENTARY MATERIALS

Supplementary material for this article is available at http://advances.sciencemag.org/cgi/content/full/6/23/eaaz5132/DC1

## REFERENCES AND NOTES


1. R. J. Hemley, H.-K. Mao, *In Situ* Studies of Iron under Pressure: New windows on the Earth's Core. *Int. Geol. Rev.* **43**, 1–30 (2001).
2. L. Dubrovinsky, N. Dubrovinskaia, O. Narygina, I. Kantor, A. Kuznetzov, V. B. Prakapenka, L. Vitos, B. Johansson, A. S. Mikhaylushkin, S. I. Simak, I. A. Abrikosov, Body-centered cubic iron-nickel alloy in Earth's core. *Science* **316**, 1880–1883 (2007).
3. J. K. Wicks, R. F. Smith, D. E. Fratanduono, F. Coppari, R. G. Kraus, M. G. Newman, J. R. Rygg, J. H. Eggert, T. S. Duffy, Crystal Structure and equation of state of Fe-Si alloys at super-Earth core conditions. *Sci. Adv.* **4**, eaao5864 (2018).
4. K. Hirose, S. Labrosse, J. Hernlund, Compositon and state of the core. *Annu. Rev. Earth Planet. Sci.* **41**, 657–691 (2013).
5. P. M. Giles, M. H. Longenbach, A. R. Marder, High-Pressure α ⇄ ε Martensitic Transformation in Iron. *J. Appl. Phys.* **42**, 4290–4295 (1971).
6. R. D. Taylor, M. P. Pasternak, Hysteresis in the high pressure transformation of bcc- to hcp-iron. *J. Appl. Phys.* **69**, 6126–6128 (1991).
7. L. M. Barker, R. E. Hollenbach, Shock wave study of the α - ε phase transition in iron. *J. Appl. Phys.* **45**, 4872 (1974).
8. R. F. Smith, J. H. Eggert, D. C. Swift, J. Wang, T. S. Duffy, D. G. Braun, R. E. Rudd, D. B. Reisman, J.-P. Davis, M. D. Knudson, G. W. Collins, Time-dependence of the alpha to epsilon phase transformation in iron. *J. Appl. Phys.* **114**, 223507 (2013).
9. F. P. Bundy, Pressure-temperature phase diagram of iron to 200kbar, 900°C. *J. App. Phys.* **36**, 616 (1965).
10. A. Dewaele, V. Svitlyk, F. Bottin, J. Bouchet, J. Jacobs, Iron under conditions close to the α-γ-ε triple point. *Appl. Phys. Lett.* **112**, 201906 (2018).
11. R. F. Smith, J. H. Eggert, R. E. Rudd, D. C. Swift, C. A. Bolme, G. W. Collins, High strain-rate plastic flow in Al and Fe. *J. Appl. Phys.* **110**, 123515 (2011).
12. J. C. Jamieson, A. W. Lawson, X-ray diffraction studies in the 100 kilobar pressure range. *J. Appl. Phys.* **33**, 776–780 (1962).
13. T. Takahashi, W. A. Bassett, High-pressure polymorph of iron. *Science* **145**, 483–486 (1964).
14. J. P. Rueff, M. Krisch, Y. Q. Cai, A. Kaprolat, M. Hanfland, M. Lorenzen, C. Masciovecchio, R. Verbeni, F. Sette, Magnetic and structural α-ε phase transition in Fe monitored by x-ray emission spectroscopy. *Phys. Rev. B* **60**, 14510 (1999).
15. J. M. Walsh, Metal equation of state from shock-wave studies. *Bull. Am. Phys. Soc.* **29**, 28 (1954).
16. D. Bancroft, E. L. Peterson, S. Minshall, Polymorphism of iron at high pressure. *J. Appl. Phys.* **27**, 291–298 (1956).
17. K. Kadau, T. C. Germann, P. S. Lomdahl, B. L. Holian, Atomistic simulations of shock-induced transformations and their orientation dependence in bcc Fe single crystals. *Phys. Rev. B* **72**, 064120 (2005).
18. K. Kadau, T. C. Germann, P. S. Lomdahl, B. L. Holian, Microscopic view of structural phase transitions induced by shock waves. *Science* **296**, 1681–1684 (2002).
19. B. J. Jensen, G. T. Gray III, R. S. Hixson, Direct measurements of the α – ε transition stress and kinetics for shocked iron. *J. Appl. Phys.* **105**, 103502 (2009).
20. D. H. Kalantar, J. F. Belak, G. W. Collins, J. D. Colvin, H. M. Davies, J. H. Eggert, T. C. Germann, J. Hawreliak, B. L. Holian, K. Kadau, P. S. Lomdahl, H. E. Lorenzana, M. A. Meyers, K. Rosolankova, M. S. Schneider, J. Sheppard, J. S. Stölken, J. S. Wark, Direct observation of the α-ε transition in shock-compressed iron via nanosecond x-ray diffraction. *Phy. Rev. Let.* **95**, 075502 (2005).
21. Q. Johnson, A. Mitchell, R. N. Keeler, L. Evans, X-ray diffraction during shock-wave compression. *Phys. Rev. Lett.* **25**, 1099 (1970).
22. Q. Johnson, A. Mitchell, L. Evans, X-ray diffraction evidence for crystalline order and isotropic compression during the shock-wave process. *Nature* **231**, 310–311 (1971).
23. Q. Johnson, A. Mitchell, L. Evans, X-ray diffraction study of single crystals undergoing shock-wave compression. *Appl. Phys. Lett.* **21**, 29 (1972).
24. J. S. Wark, R. R. Whitlock, A. A. Hauer, J. E. Swain, P. J. Solone, Sub nanosecond x-ray diffraction from laser-shocked crystals. *Phys. Rev. B* **40**, 5705 (1989).

25. J. Hawreliak, J. D. Colvin, J. H. Eggert, D. H. Kalantar, H. E. Lorenzana, J. S. Stölken, H. M. Davies, T. C. Germann, B. L. Holian, K. Kadau, P. S. Lomdahl, A. Higginbotham, K. Rosolankova, J. Sheppard, J. S. Wark, Analysis of the x-ray diffraction signal for the α - ϵ transition in shock-compressed iron: Simulation and experiment. *Phys. Rev. B* **74**, 184107 (2006).
26. D. H. Kalantar, J. Belak, E. Bringa, K. Budil, M. Caturla, J. Colvin, M. Kumar, K. T. Lorenz, R. E. Rudd, J. Stölken, A. M. Allen, K. Rosolankova, J. S. Wark, M. A. Meyers, M. Schneider, High-pressure, high-strain-rate lattice response of shocked materials. *Phys. Plasmas* **10**, 1569 (2003).
27. D. H. Kalantar, E. Bringa, M. Caturla, J. Colvin, K. T. Lorenz, M. Kumar, J. Stölken, A. M. Allen, K. Rosolankova, J. S. Wark, M. A. Meyers, M. Schneider, T. R. Boehly, Multiple film plane diagnostic for shocked lattice measurements. *Rev. Sci. Instrum.* **74**, 1929 (2003).
28. M. Bastea, S. Bastea, R. Becker, High pressure phase transformation in iron under fast compression. *Appl. Phys. Lett.* **95**, 241911 (2009).
29. J. C. Crowhurst, B. W. Reed, M. R. Armstrong, H. B. Radousky, J. A. Carter, D. C. Swift, J. M. Zaug, R. W. Minich, N. E. Teslich, M. Kumar, The α→ϵ phase transition in iron at strain rates up to ~$10^9$ $s^{-1}$. *J. Appl. Phys.* **115**, 113506 (2014).
30. K. Kadau, T. C. Germann, P. S. Lomdahl, R. C. Albers, J. S. Wark, A. Higginbotham, B. L. Holian, Shock Waves in Polycrystalline Iron. *Phys. Rev. Lett.* **98**, 135701 (2007).
31. S. J. Tracy, R. F. Smith, J. K. Wicks, D. E. Frantanduono, A. E. Gleason, C. A. Bolme, V. B. Prakapenka, S. Speziale, K. Appel, A. Fernandez-Pañella, H. J. Lee, A. MacKinnon, F. Tavella, J. H. Eggert, T. S. Duffy, *In-situ* observation of a phases transition in silicon carbide under shock compression using pulsed x-ray diffraction. *Phys. Rev. B* **99**, 214106 (2019).
32. Y. Ihm, D. H. Cho, D. Sung, D. Nam, C. Jung, T. Sato, S. Kim, J. Park, S. Kim, M. Gallagher-Jones, Y. Kim, R. Xu, S. Owada, J. H. Shim, K. Tono, M. Yabashi, T. Ishikawa, J. Miao, D. Y. Noh, C. Song, Direct observation of picosecond melting and disintegration of metallic nanoparticles. *Nat. Commun.* **10**, 2411 (2019).
33. C. Prescher, V. B. Prakapenka, *DIOPTAS*: A program for reduction of two-dimensional X-ray diffraction data and data exploration. *High Press. Res.* **35**, 223–230 (2015).
34. S. I. Ashitkov, V. V. Zhakhovsky, N. A. Inogamov, P. S. Komarov, M. B. Agranat, G. I. Kanel, The behavior of iron under ultrafast shock loading driven by a femtosecond laser. *AIP Conf. Proc.* **1793**, 100035 (2015).
35. J. M. Brown, J. N. Fritz, R. S. Hixson, Hugoniot data for iron. *J. Appl. Phys.* **88**, 5496–5498 (2000).
36. N. J. Hartley, N. Ozaki, T. Matsuoka, B. Albertazzi, A. Faenov, Y. Fujimoto, H. Habara, M. Harmand, Y. Inubushi, T. Katayama, M. Koenig, A. Krygier, P. Mabey, Y. Matsumura, S. Matsuyama, E. E. McBride, K. Miyanishi, G. Morard, T. Okuchi, T. Pikuz, O. Sakata, Y. Sano, T. Sato, T. Sekine, Y. Seto, K. Takahashi, K. A. Tanaka, Y. Tange, T. Togashi, Y. Umeda, T. Vinci, M. Yabashi, T. Yabuuchi, K. Yamauchi, R. Kodama, Ultrafast observation of lattice dynamics in laser-irradiated gold foils. *Appl. Phys. Lett.* **110**, 071905 (2017).
37. S. I. Ashitkov, P. S. Komarov, M. B. Agranat, G. I. Kanel, V. E. Fortov, Achievement of ultimate values of the bulk and shear strengths of iron irradiated by femtosecond laser pulses. *JETP Lett.* **98**, 384–388 (2013).
38. K. Yano, Y. Horie, Discrete-element modeling of shock compression of polycrystalline copper. *Phys. Rev. B* **59**, 13672 (1999).
39. K. E. Brown, S. D. McGrane, C. A. Bolme, D. S. Moore, Ultrafast chemical reactions in shocked nitromethane probed with dynamic ellipsometry and transient absorption spectroscopy. *J. Phys. Chem. A* **118**, 2559–2567 (2014).
40. N. N. Thadhani, R. A. Graham, T. Royal, E. Dunbar, M. U. Anderson, G. T. Holman, Shock-induced chemical reactions in titanium-silicon powder mixtures of different morphologies: Time-resolved pressure measurements and materials analysis. *J. Appl. Phys.* **82**, 1113 (1997).
41. Y. Xiong, S. Xiao, H. Deng, W. Zhu, W. Hu, Investigation of the shock-induced chemical reaction (SICR) in Ni + Al nanoparticle mixtures. *Phys. Chem. Chem. Phys.* **19**, 17607–17617 (2017).
42. M. Kim, C.-K. Min, I. Eom, Laser systems for time-resolved experiments at the pohang accelerator laboratory x-ray free-electron laser beamlines. *J. Synchrotron Rad.* **26**, 868–873 (2019).
43. H.-S. Kang, C.-K. Min, H. Heo, C. Kim, H. Yang, G. Kim, I. Nam, S. Y. Baek, H.-J. Choi, G. Mun, B. R. Park, Y. J. Suh, D. C. Shin, J. Hu, J. Hong, S. Jung, S.-H. Kim, K. H. Kim, D. Na, S. S. Park, Y. J. Park, J.-H. Han, Y. G. Jung, S. H. Jeong, H. G. Lee, S. Lee, S. Lee, W.-W. Lee, B. Oh, H. S. Suh, Y. W. Parc, S.-J. Park, M. H. Kim, N.-S. Jung, Y.-C. Kim, M.-S. Lee, B.-H. Lee, C.-W. Sung, I.-S. Mok, J.-M. Yang, C.-S. Lee, H. Shin, J. H. Kim, Y. Kim, J. H. Lee, S.-Y. Park, J. Kim, J. Park, I. Eom, S. Rah, S. Kim, K. H. Nam, J. Park, J. Park, S. Kim, S. Kwon, S. H. Park, K. S. Kim, H. Hyun, S. N. Kim, S. Kim, S.-m. Hwang, M. J. Kim, C.-y. Lim, C.-J. Yu, B.-S. Kim, T.-H. Kang, K.-W. Kim, S.-H. Kim, H.-S. Lee, H.-S. Lee, K.-H. Park, T.-Y. Koo, D.-E. Kim, I. S. Ko, Hard X-ray free-electron laser with femtosecond scale timing jitter. *Nat. Photon.* **11**, 708–713 (2017).
44. J. Park, I. Eom, T.-H. Kang, S. Rah, K. H. Nam, J. Park, S. Kim, S. Kwon, S. H. Park, K. S. Kim, H. Hyun, S. N. Kim, E. H. Lee, H. Shin, S. Kim, M. Kim, H.-J. Shin, D. Ahn, J. Lim, C.-J. Yu, C. Song, H. Kim, D. Y. Noh, H. S. Kang, B. Kim, K.-W. Kim, I. S. Ko, M.-H. Cho, S. Kim, Design of a hard X-ray beamline and end-station for pump and probe experiments at Pohang Accelerator Laboratory X-ray Free Electron Laser facility. *Nucl. Instrum. Methods Phys. Res. A* **810**, 74–79 (2016).
45. H.-S. Kang, H. Yang, G. Kim, H. Heo, I. Nam, C.-K. Min, C. Kim, S. Y. Baek, H.-J. Choi, G. Mun, B. R. Park, Y. J. Suh, D. C. Shin, J. Hu, J. Hong, S. Jung, S.-H. Kim, K. Kim, D. Na, S. S. Park, Y. J. Park, J.-H. Han, Y. G. Jung, S. H. Jeong, M. J. Kim, H. G. Lee, S. Lee, W.-W. Lee, B. Oh, H. S. Suh, K.-H. Park, H.-S. Lee, D. Z. Khan, T. O. Raubenheimer, J. Wu, FEL performance achieved at PAL-XFEL using a three-chicane bunch compression scheme. *J. Synchrotron Rad.* **26**, 1127–1138 (2019).
46. J. J. MacFarlane, I. E. Golovkin, P. R. Woodruff, HELIOS-CR - a 1-D radiation-magnetohydrodynamics code with inline atomic kinetics modeling. *J. Quant. Spectrosc. Ra.* **99**, 381–397 (2006).
47. R. M. More, K. H. Warren, D. A. Young, G. B. Zimmerman, A new quotidian equation of state (QEOS) for hot dense matter. *Phys. Fluids* **31**, 3059 (1988).
48. J. C. Boettger, D. C. Wallace, Metastability and dynamics of the shock-induced phase transition in iron. *Phys. Rev. B* **55**, 2840–2849 (1997).
49. R. Hrubiak, J. S. Smith, G. Shen, Multimode scanning X-ray diffraction microscopy for diamond anvil cell experiments. *Rev. Sci. Instrum.* **90**, 025109 (2019).


**Acknowledgments:** The x-ray experiment was performed at the beamline XSS (proposal nos. 2017-2nd-XSS-013, 2018-2nd-XSS-015, and 2019-1st-XSS-018) at PAL-XFEL funded by the MSIP. Portions of this work were performed at HPCAT (Sector 16), Advanced Photon Source (APS), Argonne National Laboratory. HPCAT operations are supported by DOE-NNSA's Office of Experimental Sciences. The Advanced Photon Source is a U.S. Department of Energy (DOE) Office of Science User Facility operated for the DOE Office of Science by Argonne National Laboratory under Contract No. DE-AC02-06CH11357. **Funding:** This work was supported by the Leader Researcher program (NRF-2018R1A3B1052042) of the Korean Ministry of Science and ICT (MSIP). We also thank the support by the NRF-2016K1A4A3914691 and NRF-2016K1A3A7A09005244 grants of the MSIP, and PE20200 funded by Korea Polar Research Institute. H.C. was supported under the auspices of the U.S. Department of Energy by the Lawrence Livermore National Laboratory under contract DE-AC52-07NA27344. H.J.L and E.G were supported by the U.S. Department of Energy, Office of Science, Office of Fusion Energy Sciences under contract DE-AC02-76SF00515. **Author contributions:** H.Hw. contributed to the experiments and data analysis with the help from Y.B., G.H., J.C., T.K., M.Ko., S.Kw., K.K., and Yongm.L. E.G. and H.J.L. helped with the experimental design; and I.E. and S.H.C. helped with beamline setup and operation with Sa.Ki., J.P., Su.Ki., D.N., J.H.L., H.Hy., M.Ki, and T.Y.K. C.P. and J.I.L. helped with the postshock analyses using EPMA. Yongj.L. designed the research and discussed the results with H.C., T.S., T.V., S.H.S., W.Y., and C.C.K. and worked on the manuscript with all the authors. **Competing interests:** The authors declare that they have no competing interests. **Data and materials availability:** All data needed to evaluate the conclusions in the paper are present in the paper and/or the Supplementary Materials. Additional data related to this paper may be requested from the authors.

Submitted 15 September 2019
Accepted 6 April 2020
Published 5 June 2020
10.1126/sciadv.aaz5132

**Citation:** H. Hwang, E. Galtier, H. Cynn, I. Eom, S. H. Chun, Y. Bang, G. Hwang, J. Choi, T. Kim, M. Kong, S. Kwon, K. Kang, H. J. Lee, C. Park, J. I. Lee, Yongmoon Lee, W. Yang, S.-H. Shim, T. Vogt, Sangsoo Kim, J. Park, Sunam Kim, D. Nam, J. H. Lee, H. Hyun, M. Kim, T.-Y. Koo, C.-C. Kao, T. Sekine, Yongjae Lee, Subnanosecond phase transition dynamics in laser-shocked iron. *Sci. Adv.* **6**, eaaz5132 (2020).

# Subnanosecond phase transition dynamics in laser-shocked iron

H. Hwang, E. Galtier, H. Cynn, I. Eom, S. H. Chun, Y. Bang, G. C. Hwang, J. Choi, T. Kim, M. Kong, S. Kwon, K. Kang, H. J. Lee, C. Park, J. I. Lee, Yongmoon Lee, W. Yang, S.-H. Shim, T. Vogt, Sangsoo Kim, J. Park, Sunam Kim, D. Nam, J. H. Lee, H. Hyun, M. Kim, T.-Y. Koo, C.-C. Kao, T. Sekine and Yongjae Lee

*Sci Adv* **6** (23), eaaz5132.
DOI: 10.1126/sciadv.aaz5132